# Pattern formation in a thread falling onto a moving belt: An "elastic sewing machine"

Mehdi Habibi,[1] Javad Najafi,[1] and Neil M. Ribe[2]

[1]*Department of Physics, Institute for Advanced Studies in Basic Sciences (IASBS), Zanjan 45137-66731, Iran*

[2]*Lab FAST (Fluides, Automatique et Systèmes Thermiques), Université Pierre et Marie Curie, Université Paris-Sud, CNRS, Bâtiment 502, Campus Universitaire, F-91405 Orsay, France*

(Received 8 February 2011; revised manuscript received 26 June 2011; published 25 July 2011)

We study the dynamics of instability and pattern formation in a slender elastic thread that is continuously fed onto a surface moving at constant speed $V$ in its own plane. As $V$ is decreased below a critical value $V_c$, the steady "dragged catenary" configuration of the thread becomes unstable to sinusoidal meanders and thence to a variety of more complex patterns including biperiodic meanders, figures of 8, "W," "two-by-one," and "two-by-two" patterns, and double coiling. Laboratory experiments are performed to determine the phase diagram of these patterns as a function of $V$, the thread feeding speed $U$, and the fall height $H$. The meandering state is quantified by measuring its amplitude and frequency as functions of $V$, which are consistent with a Hopf bifurcation. We formulate a numerical model for a slender elastic thread that predicts well the observed steady shapes but fails to predict the frequency of the onset of meandering, probably because of slippage of the thread relative to the belt. A comparison of our phase diagram with the analogous diagram for a thread of viscous fluid falling on a moving surface reveals many similarities, but each contains several patterns that are not found in the other.

DOI: 10.1103/PhysRevE.84.016219 PACS number(s): 89.75.Kd, 46.32.+x, 46.70.Hg

## I. INTRODUCTION

Slender threads, ropes, wires, cables, and rods of elastic material are ubiquitous in nature, in industry, and in the built environment: Examples include spiderwebs, vines and creepers, tree trunks and branches, telephone cables, electrical wires, reinforcement rods for concrete, ropes used by mountaineers and sailors, sewing thread, etc. The utility of all these objects depends on their ability to deform without breaking. When the forcing is weak, the resulting deformations are small and can be described by the standard textbook theory of linear elasticity. Under stronger forcing, however, slender elastic bodies can become unstable to large and complex deformations that are described by geometrically nonlinear equations, even if the material continues to obey Hooke's law [1]. Examples of such behavior include the kinking of telephone cables during laydown [2], the supercoiling of chain macromolecules such as DNA [3], helix hand reversals in plant tendrils [4], and the steady coiling of a rope falling onto a surface [5,6].

In this paper we study experimentally and theoretically a system that exhibits a particularly rich spectrum of elastic instability and pattern formation: a slender elastic thread falling onto a belt moving at constant velocity in its own plane. The stitchlike character of the patterns laid down by the thread on the belt leads us to call this system the "elastic sewing machine," by analogy to the previously studied "fluid mechanical sewing machine" in which the falling thread is a viscous fluid [7–9]. While our primary interest is fundamental, we note that both the elastic and fluid sewing machines can be regarded as idealized single-filament models for the "spunbonding" process of nonwoven fabric production, wherein a multitude of molten polymer filaments become entangled and solidify as they fall onto a moving screen [10].

Our study begins with systematic laboratory experiments to determine the phase diagram of the stitch patterns in the space of the thread feeding speed $U$, the fall height $H$, and the belt speed $V$. We also quantify the amplitude and frequency of the meandering pattern that corresponds to the first bifurcation from the steady state as $V$ decreases. Next, we propose a numerical model for the falling thread and compare its predictions of steady-state shapes and meandering frequencies with our experimental observations. Finally, we compare our phase diagrams with those of the related phenomena of steady elastic coiling and the fluid-mechanical sewing machine.

## II. EXPERIMENTAL PROCEDURE

Our experimental setup is shown in Fig. 1. A silicone thread with a diameter $d = 2a = 1$ mm and density $\rho = 1830\ \mathrm{kg\ m^{-3}}$ was wound onto a spool, which was rotated by an electric motor to feed the thread downward at a speed $U = 8$–$30\ \mathrm{cm\ s^{-1}}$. The thread passed first through a fixed ring of inner diameter 6 mm and then fell onto a moving belt 5–90 cm below the ring. The belt was made of paper 21 cm wide looped over two cylinders driven by an ac motor at constant speed $V$ (1.5–50 $\mathrm{cm\ s^{-1}}$). The speeds $U$ and $V$ were measured to within a few percent by putting ink marks on the spool and the belt and taking movies.

To measure the Young's modulus $E$ of the thread, we first eliminated its residual intrinsic curvature by suspending it with a weight attached to its lower end. We then measured the downward deflection $y$ of the free ends of horizontally clamped pieces of thread with different lengths $L$, and used least-squares regression against the analytical prediction $y = \rho g L^4/(2a^2E)$ of the linear theory of elastic rods to infer $E = 5 \pm 1$ MPa [11].

## III. EXPERIMENTAL OBSERVATIONS

For fixed values of the feed rate $U$ and the fall height $H$, we observe three distinct regimes as the belt speed $V$ decreases:

(1)"*Catenary*" *regime* ($V > U$): When $V$ significantly exceeds $U$, the thread slips continually relative to the belt, and exhibits a steady catenary shape [Fig. 2(a)]. The position of the contact point where the thread first touches the belt is nearly constant in time. When $V$ exceeds $U$ by several $\mathrm{cm\ s^{-1}}$, the

 

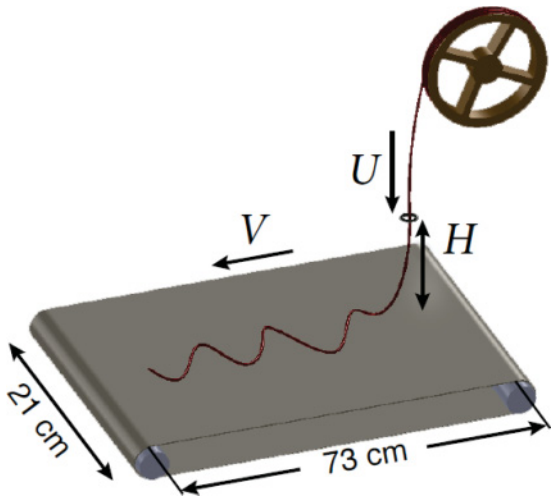


FIG. 1. (Color online) Experimental setup. A silicone thread was wound onto a wheel, which was rotated by an electric motor to feed the thread at velocity $U$ through a guide ring and thence onto a belt a distance $H$ below moving at constant speed $V$. The center of the guide ring is located $4 \pm 1$ cm from the rightmost (upstream) edge of the horizontal part of the belt.

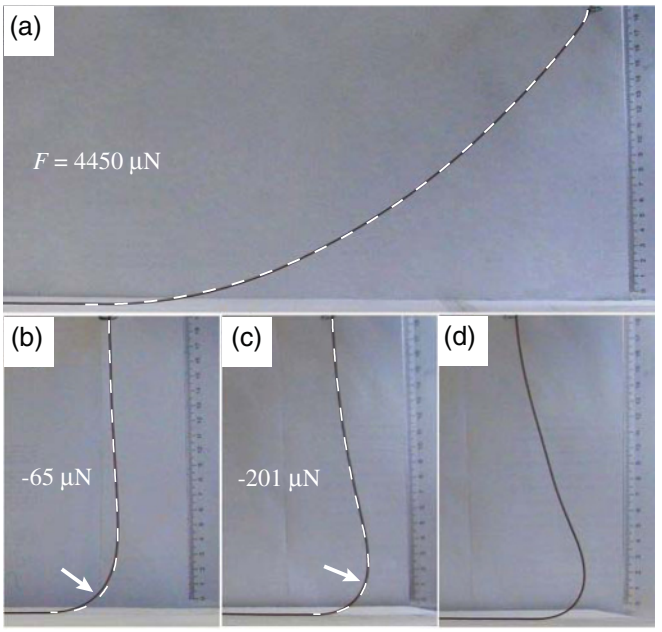


FIG. 2. (Color online) Photos of the thread (black lines) in side view, with $H = 20$ cm and $U = 10$ cm s$^{-1}$. The vertical scale at the right-hand side of each image is in cm. The belt is moving from the right-hand side to the left-hand side, and the guide ring is visible at the top of each image. (a) Catenary state ($V = 15.7$ cm s$^{-1}$). (b) Steady heel ($V = 10.3$ cm s$^{-1}$). (c) Onset of meandering ($V = 10.0$ cm s$^{-1}$). (d) Meandering ($V = 9.5$ cm s$^{-1}$). The dashed white lines are the numerically predicted shapes that best fit the observed shapes of the thread [not calculated for (d) because the thread is unsteady]. The arrows in (b) and (c) indicate where the axial state of stress changes from extensional (above) to compressional (below). The numerically predicted force $F$ exerted by the belt on the thread (positive in the direction of belt motion) is indicated.

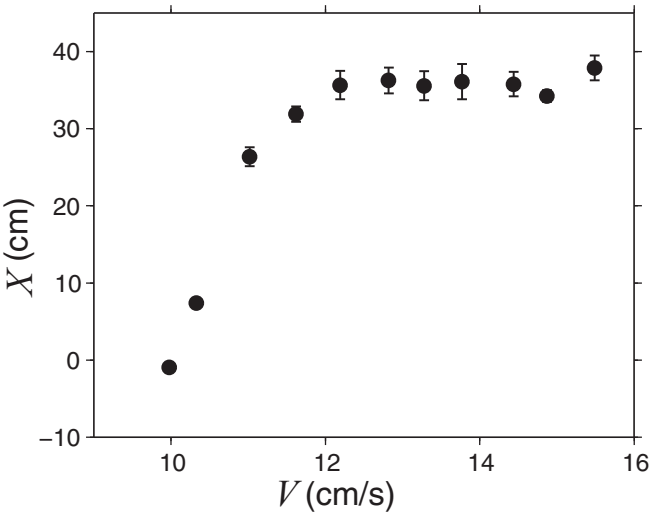


FIG. 3. Dragout distance (measured from the center of the guide ring) as a function of the belt velocity $V$, for $H = 20$ cm and $U = 10$ cm s$^{-1}$.

contact point is typically located a few tens of cm downstream from the guide ring, and its position is nearly independent of $V$ (Fig. 3, right-hand side). As $V$ decreases, however, the contact point moves progressively closer to the point below the guide ring (Fig. 3, left-hand side).

(2)"*Steady heel*" *regime* ($V \approx U$): For values of $V$ that only slightly exceed $U$, the thread develops an inflexion point where its curvature changes sign, and has the form of an upstream-facing heel [Figs. 2(b) and 2(c)]. The contact point is typically within a few cm of the horizontal position of the guide ring [Fig. 2(c)].

(3)"*Stitching*" *regime* ($V < U$): When the belt speed $V$ decreases below $U$, the thread's motion becomes unsteady, and produces a variety of complex patterns on the belt depending on the value of $V$. The first pattern to appear is a meandering state in which the contact point traces a sinusoidal path [Fig. 2(d) and Figs. 4(b)–4(d)]. A further decrease of the belt speed gives rise to new patterns, including biperiodic meanders [Figs. 4(e)–4(f)], W patterns [Fig. 4(g)], figures of 8 [Fig. 4(h)], ampersands (&) [Fig. 4(i)], W-by-8 patterns [Fig. 4(j)], "two by one" [Fig. 4(k)], "two by two" [Fig. 4(l)], and double coiling [Fig. 4(m)]. Finally, at the lowest belt speeds a translated coiling pattern is observed [Fig. 4(n)], corresponding to the last stage before stationary coiling on a motionless ($V = 0$) surface. Several transient or semirandom patterns were also observed, especially at high values of $U$ and $V$ (Fig. 5).

To understand in more detail the systematics of the observed stitch patterns, we performed two series of experiments in which the control parameters $U$ and $H$, respectively, were held fixed. In the first series, $U = 8$ cm s$^{-1}$ while $H$ was varied in the range 5–90 cm and $V$ in the range 1.5–8.5 cm s$^{-1}$. The resulting phase diagram in the $H$-$V$ plane is shown in Fig. 6. The states observed are controlled primarily by $V$. In order of increasing $V$, the dominant states are translated coiling ($V = 1.5$–$3.0$ cm s$^{-1}$), figures of 8 ($V = 3.0$–$5.5$ cm s$^{-1}$), meandering plus double meandering ($V = 5.0$–$6.5$ cm s$^{-1}$), and meandering alone ($V = 7.0$–$7.5$ cm s$^{-1}$). The W state is seen only for $V = 4.0$–$5.5$ cm s$^{-1}$, while the two-by-one

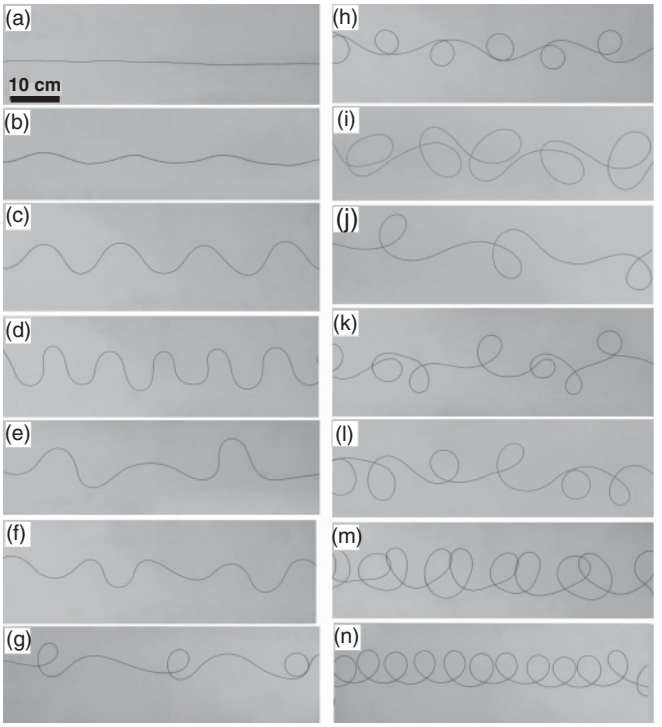


FIG. 4. Observed patterns of the thread on the belt. $U = 8$ cm s$^{-1}$ for all patterns except (i) and (j), for which $U = 30$ cm s$^{-1}$. The values of ($H$, $V$) are indicated below for each case. (a) Steady catenary (35 cm, 8 cm s$^{-1}$). (b) Meandering (70 cm, 7.5 cm s$^{-1}$). (c) Meandering (10 cm, 5.5 cm s$^{-1}$). (d) Meandering (10 cm, 4 cm s$^{-1}$). (e) Biperiodic meanders (45 cm, 6 cm s$^{-1}$). (f) Biperiodic meanders (10 cm, 5.5 cm s$^{-1}$). (g) W pattern (30 cm, 4.5 cm s$^{-1}$). (h) Figure of 8 (15 cm, 3 cm s$^{-1}$). (i) Ampersand (&) pattern (20 cm, 8 cm s$^{-1}$). (j) W by 8 (20 cm, 15 cm s$^{-1}$). (k) Two by one (30 cm, 3 cm s$^{-1}$). (l) Two by two (30 cm, 3 cm s$^{-1}$). (m) Double coil (40 cm, 2 cm s$^{-1}$). (n) Translated coiling (10 cm, 2 cm s$^{-1}$).

and double 8 states are observed only when $V = 3.0$ cm s$^{-1}$. Irregular patterns are seen at large heights $H = 90$ cm when $V \geqslant 5.0$ cm s$^{-1}$. Finally, when $V \geqslant 8$ cm s$^{-1}$, the thread has a steady catenary shape.

In the second series of experiments we fixed $H = 20$ cm and varied $U$ (8–50 cm s$^{-1}$) and $V$ (2–50 cm s$^{-1}$) to obtain a phase diagram in the $U$-$V$ plane (Fig. 7). For all values of $U$, meandering is the first state to appear when $V$ drops below $U$, and translated coiling is the last state seen before $V$ diminishes to zero. For intermediate values of $V$, however, the states observed depend strongly on $U$. The W pattern first appears at $U = 8$ cm s$^{-1}$ and $V = 4$ cm s$^{-1}$, and the range of $V$ it occupies gradually expands as $U$ increases up to 40 cm s$^{-1}$. A similar expansion of range is observed for the irregular states, which first appear at $U = 30$ cm s$^{-1}$ and $V = 7$ cm s$^{-1}$ and become progressively more dominant as $U$ increases. States observed at only a single value of $U$ include double meandering ($U = 8$ cm s$^{-1}$), double coiling ($U = 30$ cm s$^{-1}$) and W by 8 ($U = 30$ cm s$^{-1}$.) In many of these experiments, two or more states distinct states succeed each other in time, each persisting for several oscillation periods before giving way to the next. The same is true for many of the experiments in series 1.

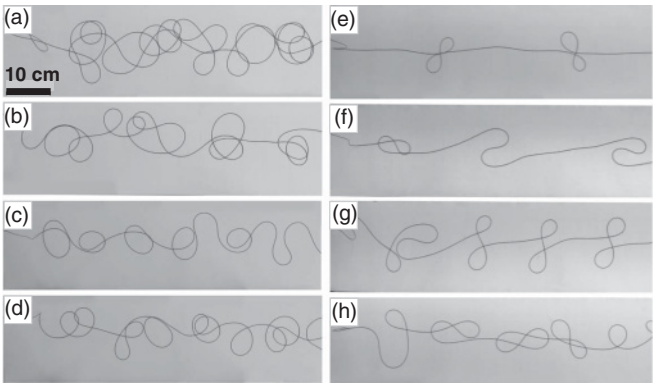


FIG. 5. Transient and semirandom patterns, mostly at high $U$ and $V$. The values of $H$, $U$, and $V$ are given for each case. (a) 20 cm, 50 cm s$^{-1}$, 7 cm s$^{-1}$. (b) 20 cm, 50 cm s$^{-1}$, 11 cm s$^{-1}$. (c) 30 cm, 8 cm s$^{-1}$, 2.5 cm s$^{-1}$. (d) 30 cm, 8 cm s$^{-1}$, 2 cm s$^{-1}$. (e) 20 cm, 90 cm s$^{-1}$, 55.1 cm s$^{-1}$. (f) 20 cm, 90 cm s$^{-1}$, 55.1 cm s$^{-1}$. (g) 20 cm, 90 cm s$^{-1}$, 31 cm s$^{-1}$. (h) 20 cm, 90 cm s$^{-1}$, 31 cm s$^{-1}$.

To quantify further the meandering state, we measured its amplitude, frequency, and wavelength as a function of the belt velocity $V$ for fixed values of $H = 20$ cm and $U = 10$ cm s$^{-1}$. The amplitude (Fig. 8) decreases with increasing $V$ and vanishes when $V = U$. The solid curve in Fig. 8 is the best-fitting Landau amplitude formula $A = \sqrt{(V_c - V)/(\mu V_c)}$ [Ref. [9], Eq. (4)], and has $V_c = 10.0$ cm s$^{-1}$ and $\mu = 0.015$ cm$^{-2}$. The good fit to the experimental observations is consistent with the interpretation that the onset of meandering is a Hopf bifurcation. Moreover, both the meandering frequency $f$ (Fig. 9) and the meandering wavelength $\lambda$ (Fig. 10) decrease as $V$ decreases. The propagation of the pattern at speed $V$ requires $f\lambda = V$, which is roughly satisfied for our experiments (Fig. 11).

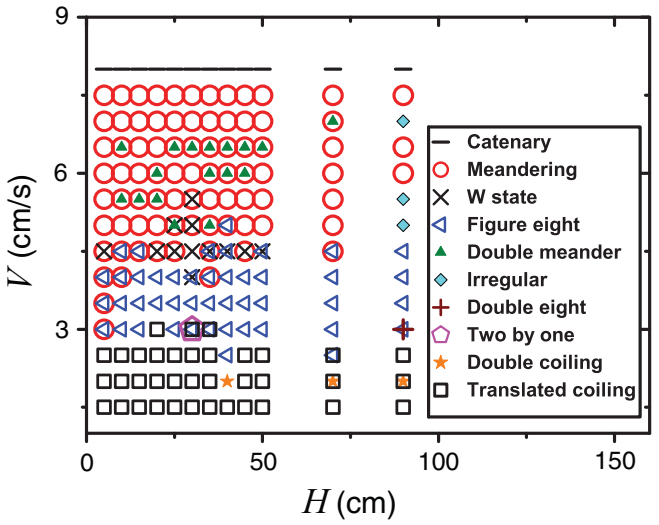


FIG. 6. (Color online) Phase diagram in the $H$-$V$ plane for $U = 8$ cm s$^{-1}$. The states are shown in Figs. 4 and 5.

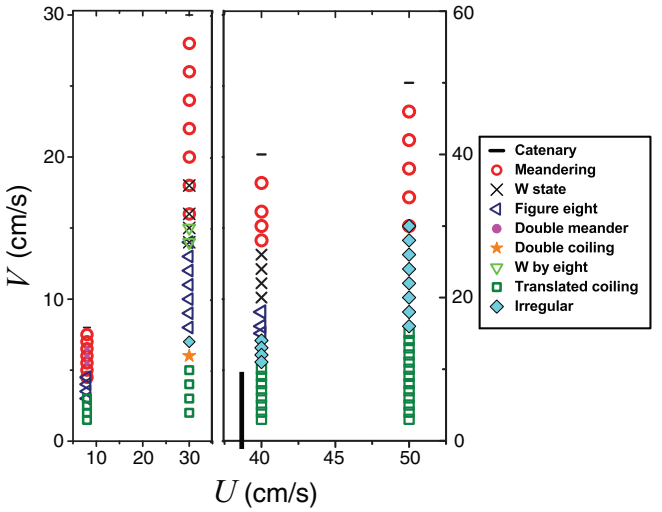


FIG. 7. (Color online) Phase diagram in the $U$-$V$ plane for $H = 20$ cm. The states are shown in Figs. 4 and 5. The vertical black bar at $U = 38.6$ cm s$^{-1}$ indicates the transition between the gravitational (G) and inertial (I) regimes of steady coiling (Fig. 12). Note the difference of vertical scale between the left-hand and right-hand parts of the figure.

## IV. NUMERICAL MODEL

We now try to understood some of our experimental observations using a numerical model for a falling elastic thread. We assume that the thread is inextensible, and that it has zero residual curvature in its natural (undeformed) state. We further assume that it is linearly elastic, i.e., that the bending moment within it is directly proportional to the local curvature of the centerline. However, because the deformation of the thread is large and not known in advance, the governing

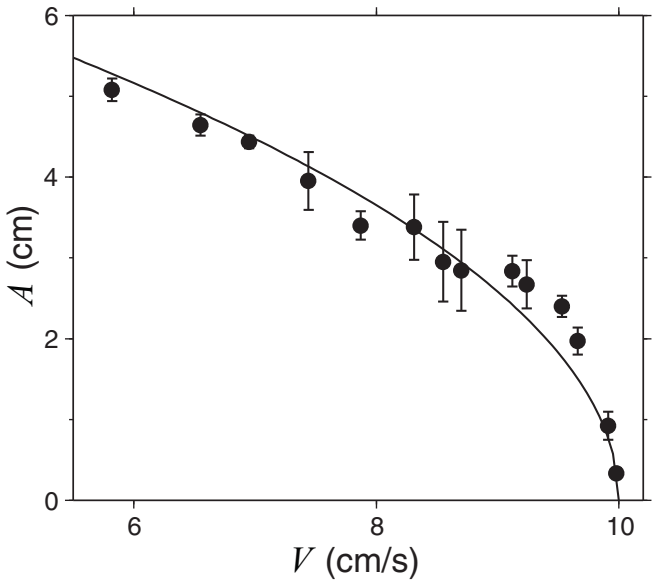


FIG. 8. Amplitude of meandering as a function of the belt speed $V$, for $H = 20$ cm and $U = 10$ cm s$^{-1}$. The solid line is $A = \sqrt{(V_c - V)/(\mu V_c)}$ with $V_c = 10.0$ cm s$^{-1}$ and $\mu = 1.5 \times 10^{-2}$ cm$^{-2}$.

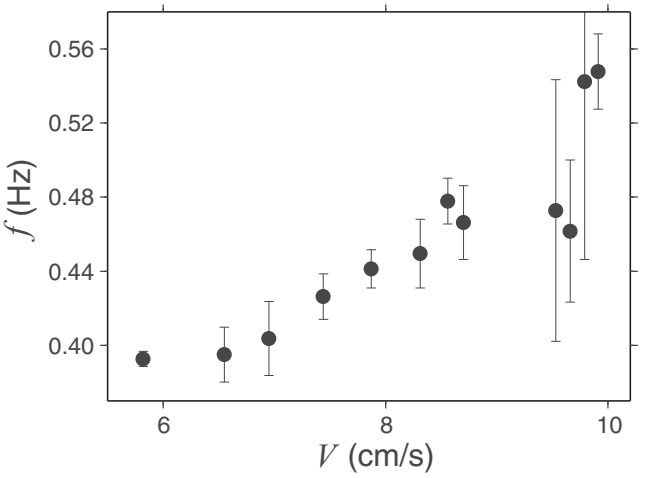


FIG. 9. Frequency of meandering as a function of the belt speed $V$, for $H = 20$ cm and $U = 10$ cm s$^{-1}$.

equations are geometrically nonlinear even though the elastic constitutive law is linear. The required equations are those of the Kirchhoff theory of elastic rods [1,11], and are written down explicitly in Appendix A. In principle, they can be used to answer three questions: (1) What are the possible steady-state shapes of a thread falling on a moving belt? (2) Under what conditions are those shapes unstable to small perturbations? And (3) if a steady solution is unstable, what is its finite-amplitude behavior far beyond the instability threshold? In this paper we consider only questions (1) and (2), leaving (3) for future work.

The steady shape of the thread depends on $\rho$, $E$, $a$, $H$, $U$, and $V$. Of these parameters, the first five appear explicitly in either the governing equations or the boundary conditions satisfied by the thread (Appendix A). The belt speed $V$, by contrast, appears nowhere explicitly, and in particular not in the boundary conditions at the contact point, where one might expect it. The reason is that the thread is an inextensible elastic

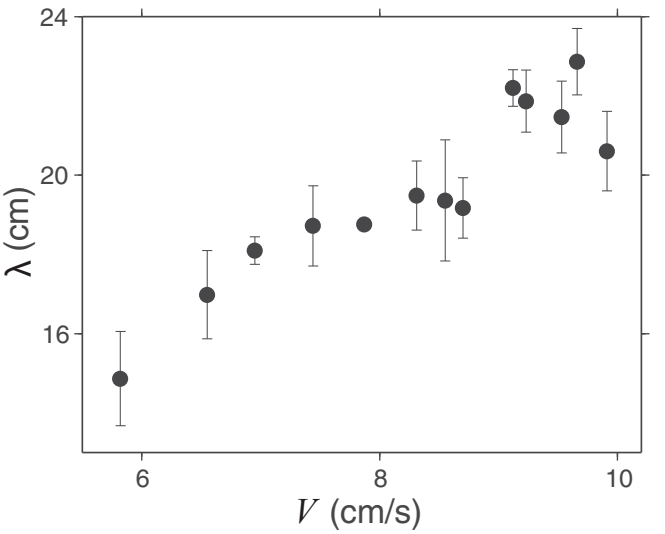


FIG. 10. Wavelength of meandering as a function of the belt speed $V$, for $H = 20$ cm and $U = 10$ cm s$^{-1}$.

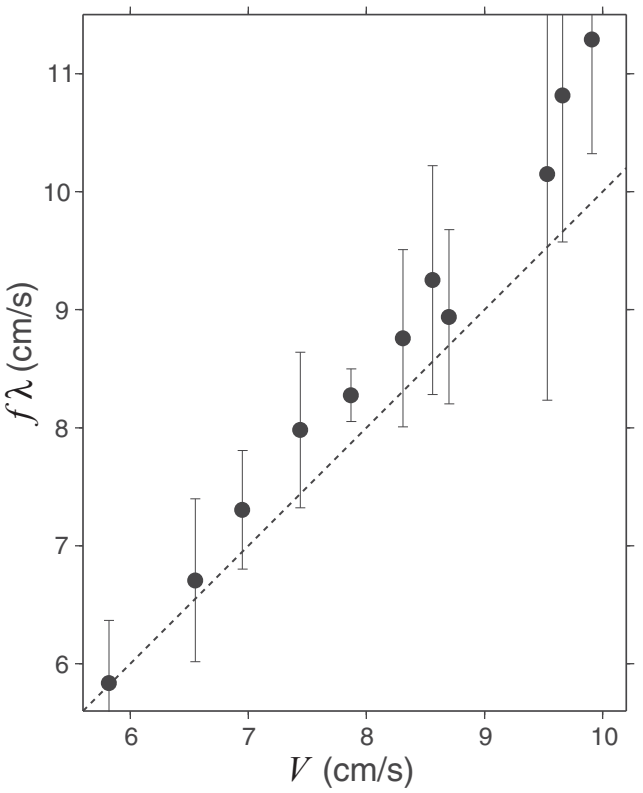


FIG. 11. Product of the meandering frequency and wavelength as a function of the belt speed $V$, for $H = 20$ cm and $U = 10$ cm s$^{-1}$. The dashed line is $f\lambda = V$.

object which can slip relative to the belt, so that its velocity at the contact point need not equal $V$. Instead, the role of the belt speed is to control (in concert with other factors such as the thread's elasticity) the horizontal frictional force $F$ that the belt exerts on the thread. The parameter $F$, rather than $V$, therefore appears explicitly in the boundary conditions at the contact point. Unlike $V$, however, $F$ cannot be measured in our experiments, and so we treat it as an unknown free parameter. The dependence of $F$ on $V$ is discussed further in Appendix B.

Figures 2(a)–2(c) show the steady shapes (white dashed lines) predicted numerically for three different vaues of $F$ for a thread with $H = 20$ cm, $U = 10$ cm s$^{-1}$ and the experimental values of $\rho$, $E$, and $a$. The values of $F$ indicated were chosen to give the best fit of the numerically predicted shapes to the shapes observed experimentally (black lines). The shapes were calculated assuming that the thread is clamped at the guide ring, but the results are hardly different if a freely hinged condition is assumed, as will be seen below. When $F = 4450$ $\mu$N, the thread has a catenary shape, and the axial stress within it is extensional everywhere. The upper part of the thread becomes progressively more vertical as $F$ diminishes. As $F$ decreases further and changes sign, the thread develops a heel-shaped structure in which elastic bending stresses are important [$F = -65$ $\mu$N and $-201$ $\mu$N; Figs. 2(b) and 2(c)]. The axial stress in the lower part of the thread [below the white arrows in Figs. 2(b) and 2(c)] is then compressive, which is a necessary condition for instability.

We now apply the numerical model to analyze the linear stability of the steady states determined above, using the method described in Appendix A to determine the complex growth rate $\sigma$ of an infinitesimal perturbation. The marginally stable state is determined by varying $F$ until $\mathrm{Re}(\sigma) = 0$, at which point $\mathrm{Im}(\sigma) \equiv 2\pi f$ should correspond to the observed frequency $f$ at the onset of meandering. Unfortunately, the agreement with our experimental measurements is poor. For the case $H = 20$ cm and $U = 10$ cm s$^{-1}$, for example, the measured onset frequency is $f_{\mathrm{obs}} \approx 0.56$ Hz (Fig. 9). By contrast, the stability analysis predicts $f_{\mathrm{num}} = 1.37$ Hz if the thread is assumed to be clamped at the guide ring, and $f_{\mathrm{num}} = 1.34$ Hz if it is hinged there. Moreover, the predicted marginally stable steady state does not match well the observed shape of the thread when meandering begins. For example, the predicted marginally stable state for the clamped case has $F = -74$ $\mu$N, whereas the observed one is best fit with $F = -201$ $\mu$N [Fig. 2(c)]. We speculate that these discrepancies may be due to slippage of the thread relative to the belt.

Next we discuss the connection of our experimental observations with the related phenomenon of steady coiling of an elastic thread falling onto a motionless surface. This comparison is motivated by the close analogy that has previously been demonstrated between viscous fluid threads falling on motionless ($V = 0$ [13–18]) and moving ($V > 0$) surfaces [7–9,19]. In particular, for given values of the flow rate, viscosity, and fall height, the frequency of steady viscous coiling with $V = 0$ is nearly identical to the onset frequency of meandering when $V = V_c$, indicating that the boundary layers in which the bending stresses are concentrated have similar structures in both cases [8,19].

A complete phase diagram for steady elastic coiling was determined by Ref. [6] as a function of the dimensionless fall height $\hat{H} = H(\rho g/d^2 E)^{1/3}$ and the dimensionless feed rate $\hat{U} = U(\rho/d^2 g^2 E)^{1/6}$ (Fig. 12). Coiling can occur in

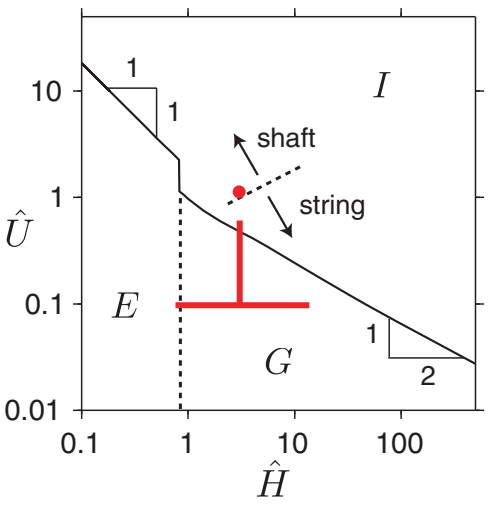


FIG. 12. (Color online) Phase diagram for steady elastic coiling in the space of dimensionless fall height $\hat{H} = H(\rho g/d^2 E)^{1/3}$ and dimensionless feed rate $\hat{U} = U(\rho/d^2 g^2 E)^{1/6}$ [6]. The different coiling regimes are indicated: elastic (E), gravitational (G), inertial (I), and the whirling-string and whirling-shaft subdivisions of the inertial regime. The ranges of values of $\hat{H}$ and $\hat{U}$ for the experiments in this paper are indicated in red.

three different regimes: (1) elastic (E), in which both gravity and inertia are negligible relative to the elastic forces in the deformed thread; (2) gravitational (G), wherein the elastic forces are balanced by gravity; and (3) inertial (I), in which the elastic forces are balanced by inertia. The inertial regime is further divided into a "whirling string" regime in which the upper part of thread has negligible bending resistance, and a "whirling shaft" regime in which the centrifugal and elastic bending forces are in balance. For comparison, Fig. 12 also shows (in red) the values of $(\hat{H},\hat{U})$ for our elastic sewing machine experiments. Most of these fall in the gravitational (G) regime. In particular, this includes all the experiments of Fig. 4, indicating the remarkable variety of patterns that can be obtained even when inertia is negligible. By contrast, all the experiments in Fig. 5 except Figs. 5(c) and 5(d) are in the inertial regime, which is consistent with the transient and/or semirandom character of the observed patterns. We note also that the boundary between the gravitational and inertial coiling regimes for $H = 20$ cm (vertical black bar in Fig. 7) corresponds well with the significant appearance of irregular patterns.

## V. COMPARISON WITH THE "FLUID MECHANICAL SEWING MACHINE"

In conclusion, we compare the behavior of our experimental system with that of a thin thread of viscous fluid falling onto a moving belt. This system was first studied experimentally by the authors of Ref. [7], who observed that the falling thread became unstable to a meandering instability when the belt speed $V$ dropped below a critical value $V_c$ that depended on the fall height, the flow rate, and the fluid viscosity. For $V < V_c$, the authors of Ref. [7] found that the thread traced out a variety of complex "stitch" patterns, many strongly resembling those of our Fig. 4. They also proposed a mathematical model for the catenary state of the thread neglecting bending forces, and showed that the criterion for the nonexistence of the solution corresponded fairly well with the observed onset of meandering. A more complete mathematical model incorporating bending forces was presented by the authors of Ref. [8], who showed that its predictions for the onset of meandering agreed closely with experimental observations. Improved experiments were performed by the authors of Ref. [9], who determined a complete phase diagram of the patterns as a function of $V$ and $H$ for a particular choice of the flow rate and the viscosity and derived generic amplitude equations that can be used to model the transition from meandering to more complicated patterns.

Despite the similar geometries of the elastic and fluid sewing machines, there are several significant differences. First, a viscous thread falling from a sufficient height is strongly stretched by gravity, so that its axial velocity $U(s)$ increases downward from the injection point. The natural free-fall velocity $U_{\text{free}}$ of the thread at a distance $H$ below the injection point therefore increases with $H$, whereas $U_{\text{free}} \equiv U$ is constant for an elastic thread. Second, a viscous thread must satisfy the no-slip condition at the moving belt, even though $U_{\text{free}}$ is not in general equal to the belt speed $V$. A viscous thread adjusts to the difference either by stretching (if $V > U_{\text{free}}$) or by buckling (if $V < U_{\text{free}}$), whereas an elastic thread slips relative to the belt if $V > U$. Third, the forces that resist the bending of a viscous thread are proportional to the rate of change of the curvature of the thread's axis, rather than to the curvature itself as for an elastic thread.

The recognition that $H$ is essentially a proxy for $U_{\text{free}}$ for a viscous thread permits us to make some illuminating qualitative comparisons between our elastic $U$-$V$ phase diagram (7) and the viscous $H$-$V$ phase diagram (Ref. [9], Fig. 3). In the remarks that follow, we refer to small (large) values of $H$ in the viscous phase diagram as "small (large) values of $U$" to emphasize the analogy with the elastic case.

As $V$ is decreased to its critical value $V_c$, the first bifurcation is almost always to the meandering state for both viscous and elastic threads. The only exception is for viscous threads at high $U$, for which double meanders sometimes appear first. At the other extreme of very small $V$, translated coiling is nearly always observed, except for viscous threads at high $U$ for which the pattern is irregular. In between these two extremes, the two phase diagrams have some striking similarities. The figure of 8 is the dominant pattern at low values of $U$ and for values of $V$ intermediate between those where meandering (higher $V$) and translated coiling (lower $V$) occur, and is not observed for intermediate values of $U$. Second, double coiling and the W pattern are rare and are confined to a narrow intermediate range of values of $U$. Finally, irregular patterns make their first appearance at intermediate values of $U$ and become progressively more dominant (i.e., are observed over a wider range of values of $V$) as $U$ increases. However, there are also some significant differences. First, the figure of 8 reappears at high values of $U$ for viscous threads, but apparently not for elastic ones. Second, double meanders are seen only for low $U$ for viscous threads, but only at high $U$ for elastic threads. Finally, some patterns are common in one case and rare or nonexistent in the other. Patterns observed only for viscous threads include bunched meanders, braids, and slanted loops (Ref. [7], Fig. 4). By contrast, patterns such as the ampersand, W by 8, two by one, and two by two (Fig. 4) exist only for elastic threads. Some of these differences may be due to the fact that viscous and elastic threads behave very differently during self-contact, which is surface tension dominated in the former case but frictional in the latter.

A final point of comparison between the elastic and fluid cases is the dependence of the meandering amplitude $A$ on the belt speed $V$. Our Figs. 8 and 4 of Ref. [9] show that $A = \sqrt{(V_c - V)/(\mu V_c)}$ for both elastic and fluid threads, where $V_c$ is the critical belt speed and $\mu$ is a Landau coefficient. In the fluid case, the experimentally inferred value of $\mu$ is well predicted by a simple kinematic model due to Ref. [9], which is based on the assumption that the absolute speed of the meandering contact point relative to the belt always equals $V_c$. This model predicts $\mu = (\omega_c/2V_c)^2$, where $\omega_c$ is the angular frequency of meandering at onset. To judge whether this prediction matches our observations, we use the data from the experiments with $H = 20$ cm and $U = 10$ cm s$^{-1}$. The critical belt speed is $V_c = 10$ cm s$^{-1}$ for this case, and Fig. 9 gives $\omega_c = 3.44$ s$^{-1}$. The kinematic model then predicts $\mu = 0.0296$ cm$^{-2}$, approximately twice the value (0.015 cm$^{-2}$) determined by fitting the amplitude data of Fig. 8. Again, we suspect that this discrepancy may be due to slip of

the thread relative to the belt, an effect that does not exist in the fluid case.


## ACKNOWLEDGMENTS

The experiments were done in the Complex Fluid Laboratory of IASBS. The authors gratefully acknowledge support from the IASBS Research Council (Grant No. G2010IASBS103) and from the ANR (Grant PTECTO) and INSU (SEDIT program) in France. We thank an anomymous referee for constructive comments.


## APEENDIX A: DETAILS OF THE NUMERICAL MODEL

Consider a thin elastic thread with constant radius $a$, cross-sectional area $A \equiv \pi a^2$, and moment of inertia $I \equiv \pi a^4/4$. Let $s$ be the arclength coordinate along the thread's axis, and consider the portion of the thread extending from the guide ring ($s = 0$) to its point of contact $s = \ell(t)$ with the moving belt, where $t$ is time. Let $\boldsymbol{e}_i$ be Cartesian unit vectors in the laboratory frame, defined so that $\boldsymbol{e}_3$ is upward and the belt moves in the $\boldsymbol{e}_1$ direction. Let $\boldsymbol{x}(s,t)$ be the position of the thread's axis, $\boldsymbol{d}_3(s,t)$ be the unit vector tangent to the axis, and $\boldsymbol{d}_1(s,t)$ and $\boldsymbol{d}_2(s,t) \equiv \boldsymbol{d}_3(s,t) \times \boldsymbol{d}_1(s,t)$ be orthogonal unit vectors in the plane of the thread's cross section. The local orientation of the basis $\boldsymbol{d}_i$ relative to the laboratory basis $\boldsymbol{e}_j$ is described by the direction cosines $d_{ij} \equiv \boldsymbol{d}_i \cdot \boldsymbol{e}_j$. While $d_{ij}$ can be written in terms of the familiar Eulerian angles, it is more convenient for numerical purposes to use the four "Euler parameters" $q_0$, $q_1$, $q_2$, and $q_3$ [Ref. [14], Eq. (2.2)].

The rates of change of $\boldsymbol{x}$ and $\boldsymbol{d}_i$ along the thread's axis are

$$\boldsymbol{x}' = \boldsymbol{d}_3, \quad \boldsymbol{d}_i' = \boldsymbol{\kappa} \times \boldsymbol{d}_i, \tag{A1}$$

where $\boldsymbol{\kappa} \equiv \kappa_i \boldsymbol{d}_i$ is the curvature vector and primes denote differentiation with respect to $s$. In the following, Latin subscripts (e.g., $i$) take on values 1, 2, or 3, Greek subscripts (e.g., $\alpha$) take on values 1 or 2, and summation over repeated subscripts is implied. The elastic force acting on each cross section of the thread is $\boldsymbol{N}(s,t) \equiv N_i \boldsymbol{d}_i$, and the vector of bending ($M_1$,$M_2$) and twisting ($M_3$) moments is $\boldsymbol{M}(s,t) \equiv M_i \boldsymbol{d}_i$. Conservation of momentum in the thread requires

$$\rho A \ddot{\boldsymbol{r}} = \boldsymbol{N}' + A\rho \boldsymbol{g}, \tag{A2}$$

where $\ddot{\boldsymbol{r}}$ is the acceleration of the thread's axis and $\boldsymbol{g}$ is the gravitational acceleration. Conservation of angular momentum requires

$$\boldsymbol{M}' = -\boldsymbol{d}_3 \times \boldsymbol{N}, \tag{A3}$$

where the (small) effect of inertia has been neglected. Finally, the constitutive relations for the bending moments $M_\alpha$ are

$$M_\alpha = EI\kappa_\alpha. \tag{A4}$$

Now in view of (A4), the $\boldsymbol{d}_3$ component of (A3) becomes simply $M_3' = 0$. Because no twist is applied to either end of the thread, this implies $M_3 = 0$ for all $s$.

Consider now the steady state of a thread dragged by a moving belt. The thread's axis is confined to the plane $x_2 = 0$, and its local inclination from the horizontal can be described by a single angle $\bar{\theta}(s)$, or equivalently by the Euler parameters

$$\bar{q}_1 = -\cos\left(\frac{\bar{\theta}}{2} + \frac{\pi}{4}\right), \quad \bar{q}_3 = -\sin\left(\frac{\bar{\theta}}{2} + \frac{\pi}{4}\right), \tag{A5a}$$

$$\bar{q}_0 = \bar{q}_2 = 0. \tag{A5b}$$

Here and henceforth, an overbar indicates that the variable in question pertains to the steady state. The sixth-order system of equations governing this state is

$$\bar{x}_1' = \cos\bar{\theta}, \quad \bar{x}_3' = \sin\bar{\theta}, \quad \bar{\theta}' = \bar{\kappa}_2, \tag{A6a}$$

$$\bar{N}_1' = -\bar{\kappa}_2\bar{N}_3 + \rho g A\cos\bar{\theta} + \rho A\bar{\kappa}_2 U^2, \tag{A6b}$$

$$\bar{N}_3' = \bar{\kappa}_2\bar{N}_1 + \rho g A\sin\bar{\theta}, \quad \bar{\kappa}_2' = -\frac{\bar{N}_1}{EI}. \tag{A6c}$$

The appropriate boundary conditions depend on whether the thread is assumed to be clamped ($\beta = 0$) or hinged ($\beta = 1$) at the guide ring, and are

$$\bar{x}_1(0) = \bar{x}_3(0) = (1-\beta)\left[\bar{\theta}(0) + \frac{\pi}{2}\right] + \beta\bar{\kappa}_2(0) = 0, \tag{A7a}$$

$$\bar{x}_3(\bar{\ell}) + H - a = \bar{\theta}(\bar{\ell}) = \bar{\kappa}_2(\bar{\ell}) = 0. \tag{A7b}$$

The condition $\bar{\kappa}_2(\bar{\ell}) = 0$ is the "rolling" condition required for the contact point to move relative to the belt [20].

The six boundary conditions (A7) are sufficient for the system (A6) only if the thread's length $\bar{\ell}$ is known. This, however, is not the case for the sewing machine configuration, for which $\bar{\ell}$ is determined by the axial force $\bar{N}_3(\bar{\ell}) \equiv F$ applied by the belt to the thread at the point of contact. Figure 2 shows numerical solutions of (A6) and (A7) obtained for three different values of $F$ using a continuation method implemented by the software package AUTO-07P [21].

Next, we examine the stability of the steady solutions described above to small perturbations. Two distinct (and uncoupled) modes of instability are possible: an "in-plane" mode in which the thread is confined to the plane $x_2 = 0$, and an "out-of-plane" mode in which it is not. Here we consider only the out-of-plane mode, which corresponds to the meandering instability observed in our experiments. The nonzero variables for this mode are $\hat{x}_2$, $\hat{q}_0$, $\hat{q}_2$, $\hat{N}_2$, and $\hat{\kappa}_1$, where carets indicate that the variables are perturbation quantities. The linearized equations they satisfy are

$$\hat{x}_2' = \hat{d}_{32}, \quad \hat{\kappa}_1' = \hat{N}_2/(EI), \tag{A8a}$$

$$2\hat{q}_0' = -\bar{q}_1\hat{\kappa}_1 - \bar{\kappa}_2\hat{q}_2, \quad 2\hat{q}_2' = \bar{q}_3\hat{\kappa}_1 + \bar{\kappa}_2\hat{q}_0, \tag{A8b}$$

$$\hat{N}_2' = \bar{N}_3\hat{\kappa}_1 + \rho g A\hat{d}_{23} - \rho A(U^2\hat{\kappa}_1 + 2U\sigma\hat{d}_{32} + \sigma^2\hat{x}_2), \tag{A8c}$$

where $\sigma$ is the exponential growth rate of the perturbations and

$$\hat{d}_{32} = 2(\bar{q}_3\hat{q}_2 - \bar{q}_1\hat{q}_0), \quad \hat{d}_{23} = 2(\bar{q}_1\hat{q}_0 + \bar{q}_3\hat{q}_2). \tag{A9}$$

The appropriate boundary conditions are

$$\hat{x}_2(0) = (1-\beta)\hat{q}_0(0) + \beta\hat{\kappa}_1(0) = \hat{q}_2(0) = 0, \tag{A10a}$$

$$\hat{\kappa}_1(\bar{\ell}) = 0, \tag{A10b}$$

$$\sigma\hat{x}_2(\bar{\ell}) + U\hat{d}_{32}(\bar{\ell}) = 0, \tag{A10c}$$

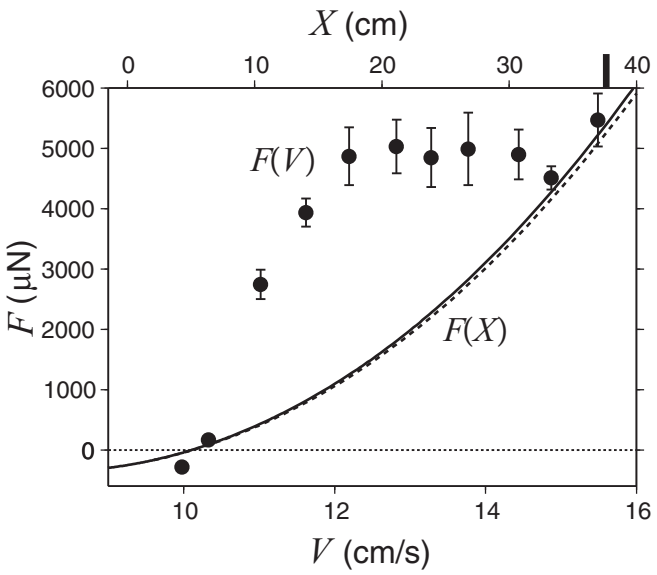


FIG. 13. Force on the thread as a function of dragout distance $X$ (upper scale) and belt speed $V$ (lower scale) for $H = 20$ cm and $U = 10$ cm s$^{-1}$. $F(X)$ was calculated numerically as described in Appendix A, assuming that the thread was clamped (solid line) or hinged (dashed line) at the guide ring. The points $F(V)$ are obtained by eliminating the variable $X$ between the solid line and the points in Fig. 3. The vertical black bar at the upper right-hand side indicates the largest value of $X$ observed in this set of experiments.

where (to repeat) $\beta = 0$ if the thread is assumed to be clamped at the guide ring and $\beta = 1$ if it is hinged. Condition (A10b) states that there is no bending moment at the contact point, and (A10c) is the $x_2$ component of the no-slip condition. Equations (A8) and (A10) constitute a linear eigenvalue problem for the complex growth rate $\sigma$, which we solved using the method of Ref. [17]. For a given steady-state solution, this method yields the spectrum of values of $\sigma$ and the associated eigenmodes $[\hat{x}_2(s), \hat{q}_0(s), \hat{q}_2(s), \hat{N}_2(s), \hat{\kappa}_1(s)]$. Once a value of $\sigma$ with $\mathrm{Re}(\sigma) > 0$ is found, a marginally stable mode is found using a continuation procedure, wherein the steady-state solution and the associated eigenmodes are gradually changed by varying $F$ until $\mathrm{Re}(\sigma) = 0$.

## APEENDIX B: FORCE ON THE DRAGGED THREAD

Because the thread can slip relative to the belt, it is of interest to examine how the horizontal force $F$ on it depends on the belt speed $V$ in the steady-state (dragged catenary) configuration. Because $F$ cannot be easily measured, an indirect procedure is

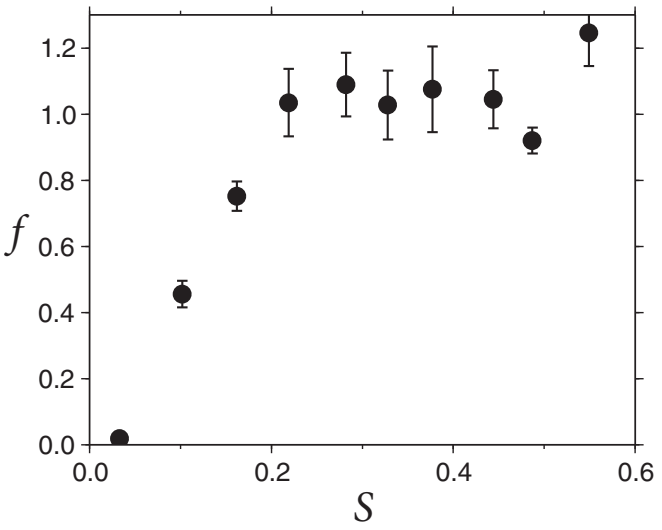


FIG. 14. Friction coefficient $f(S)$ in (B1), determined from the experiments with $H = 20$ cm and $U = 10$ cm s$^{-1}$.

required. Our approach was to eliminate the dragout distance $X$ between the experimentally measured function $X(V)$ and the function $F(X)$ predicted theoretically using the model described in Appendix A, assuming that the thread is clamped at the guide ring. Figure 13 shows the results for the measured values of $X(V)$ from Fig. 3. The force $F$ increases from values near zero when $V = U = 10$ cm s$^{-1}$ to an asymptotic value $F_\infty \approx 5000$ $\mu$N for $V > 12.5$ cm s$^{-1}$. For comparison, the dashed line shows $F(X)$ calculated assuming a hinged thread at the guide ring. The difference is very small.

We now propose that the function $F(V)$ in Fig. 13 is an example of a more general law of the form

$$F = \pi a^2 L \rho g f(S), \quad S = \frac{V - U}{U} \tag{B1}$$

where $L$ is the length of part of the thread in contact with the belt, $\pi a^2 L \rho g$ is its weight, and $S$ is the dimensionless rate of slip of the thread relative to the belt. It is well known that the variable $S$ controls dynamic friction in mechanical systems such as automobile tires on roads [22], and that the friction coefficient $f(S)$ is highly nonlinear in general. Figure 14 shows $f(S)$ for the experiments with $H = 20$ cm and $U = 10$ cm s$^{-1}$, calculated from (B1) with $L = L_0 - X$, where $L_0 = 0.69$ m (Fig. 1) and $X(V)$ is given by Fig. 3. The curve strongly resembles the force versus slip curves of Ref. [22], which increase linearly for small $S$ and saturate to a nearly constant value for $S > 0.3$.

[1] A. Goriely and M. Tabor, Nonlin. Dyn. **21**, 101 (2000).
[2] J. Coyne, IEEE J. Oceanic Eng. **15**, 72 (1990).
[3] M. D. Barkley and B. H. Zimm, J. Chem. Phys. **70**, 2991 (1979).
[4] A. Goriely and M. Tabor, Phys. Rev. Lett. **80**, 1564 (1998).
[5] L. Mahadevan and J. B. Keller, Proc. R. Soc. London A **452**, 1679 (1996).
[6] M. Habibi, N. M. Ribe, and D. Bonn, Phys. Rev. Lett. **99**, 154302 (2007).
[7] S. Chiu-Webster and J. Lister, J. Fluid Mech. **569**, 89 (2006).
[8] N. M. Ribe, J. R. Lister, and S. Chiu-Webster, Phys. Fluids **18**, 124105 (2006).
[9] S. W. Morris, J. H. P. Dawes, N. M. Ribe, and J. R. Lister, Phys. Rev. E **77**, 066218 (2008).

[10] [http://www.reicofil.com].
[11] A. E. H. Love, *A Treatise on the Mathematical Theory of Elasticity* (Dover, New York, 1944).
[12] L. Mahadevan, W. S. Ryu, and A. D. T. Samuel, Nature (London) **392**, 140 (1998).
[13] L. Mahadevan, W. S. Ryu, and A. D. T. Samuel, Nature (London) **403**, 502 (2000).
[14] N. M. Ribe, Proc. R. Soc. London A **460**, 3223 (2004).
[15] M. Maleki, M. Habibi, R. Golestanian, N. M. Ribe, and D. Bonn, Phys. Rev. Lett. **93**, 214502 (2004).
[16] N. M. Ribe, H. E. Huppert, M. Hallworth, M. Habibi, and D. Bonn, J. Fluid Mech. **555**, 275 (2006).
[17] N. M. Ribe, M. Habibi, and D. Bonn, Phys. Fluids **18**, 084102 (2006).
[18] M. Habibi, Y. Rahmani, D. Bonn, and N. M. Ribe, Phys. Rev. Lett. **104**, 074301 (2010).
[19] M. J. Blount and J. R. Lister, J. Fluid Mech. **674**, 489 (2011).
[20] N. M. Ribe, Phys. Rev. E **68**, 036305 (2003).
[21] E. Doedel *et al.*, AUTO: Software for continuation and bifurcation problems in ordinary differential equations, [http://indy.cs.concordia.ca/auto/] (2007).
[22] J. L. Harned, L. E. Johnston, and G. Scharpf, SAE Int. **78**, 690214 (1969).